Oceanic environment changes caused the Late Ordovician extinction: evidence from geochemical and Nd isotopic composition in the Yangtze area, South China

Xiangrong Yang , Detian Yan, Tong Li, Liwei Zhang, Bao Zhang, Jie He, Haoyuan Fan and Yunfei Shangguan

Key Laboratory of Tectonics and Petroleum Resources of Ministry of Education, China University of Geosciences, Wuhan, 430074, China

Abstract

The Ordovician–Silurian (O–S) transition was a critical interval in geological history. Multiple geochemical methods are used to explore the changes in oceanic environment. The Nd isotopic compositions in the Yangtze Sea are controlled by two sources: the continental erosion and the Panthalassa Ocean. High εNd(t) values during the Katian, late Hirnantian and Rhuddanian intervals are associated with the high sea level, which resulted in less terrestrial input based on the low Ti/Al and Zr/Al ratios. In contrast, low εNd(t) values during the early Hirnantian interval are related to the sea-level fall; in this case, the exposure of submarine highs and the growth of Yangtze Oldlands could lead to more continental materials being transported into the Yangtze Sea based on high Ti/Al and Zr/Al ratios. In addition, the negative εNd(t) excursion can also be attributed to the weak circulation between the Yangtze Sea and Panthalassa Ocean when sea level was low. Furthermore, the sea-level eustacy plays a significant role in the changes in redox water conditions. The redox indices, mainly U$_{EF}$, Ce/Ce* and C$_{org}$/P$_T$, across the O–S transition show a predominance of anoxic ocean over the Yangtze Sea during the Katian, late Hirnantian and Rhuddanian intervals, and an oxygenated episode was briefly introduced during the early Hirnantian period because of the fall in sea level. The Late Ordovician biotic crisis was marked by two-phase extinction events, and the change in sea level and redox chemistry may be the important kill mechanisms.

CAMBRIDGE
UNIVERSITY PRESS

1. Introduction

The Ordovician–Silurian (O–S) transition was an interval of major changes in the Earth's biotic, climatic and environmental systems, during which the Hirnantian glaciation and the end-Ordovician mass extinction took place (Kump & Arthur, 1999; Brenchley *et al.* 2003; Chen *et al.* 2006; Hammarlund *et al.* 2012; Algeo *et al.* 2016). Such glaciation was recognized from glacial sediments in north Gondwana, and the decrease in temperature was identified using oxygen isotopes in Ordovician conodonts and the palaeothermometry of other isotopes (Ghienne, 2003; Le Heron *et al.* 2007; Trotter *et al.* 2008; Finnegan *et al.* 2011). The palaeo-ocean environment underwent intense shift and significantly impacted the global cycle of carbon during the O–S transition; as a consequence, this interval was characterized by strong positive δ^{13}C excursions that have been recognized around the world (Fan *et al.* 2009; LaPorte *et al.* 2009; Yan *et al.* 2009; Melchin *et al.* 2013).

Recently, numerous studies have focused on the changes in ocean environment and climate in the Yangtze area during the Late Ordovician period, including the ocean redox conditions, chemical weathering and tectonic orogeny. The palaeoredox proxies (e.g. Fe speciation, S isotopes, Mo isotopes, degree of pyritization, Mo–U enrichment factors) indicate a predominance of stratified, anoxic ocean on the Yangtze block during this interval, which was interrupted by a brief episode of oceanic oxygenation in the early Hirnantian (Yan *et al.* 2012; Zhou *et al.* 2015; Liu *et al.* 2016; Li *et al.* 2017). A series of works have been conducted on the Late Ordovician mass extinction, and the triggering mechanisms are under debate. One proposal is that the global cooling occurred across the O–S transition and played a significant role in driving the extinction (Yan *et al.* 2010). Zou *et al.* (2018) reconstructed the oceanic redox conditions on the Yangtze Shelf Sea, and proposed that the ocean euxinia rather than global cooling may be responsible for the extinction. Hg isotope data reported by Jones *et al.* (2017) are in accord with the assumption that volcanism triggered the extinctions. In addition, other studies have investigated the marine nitrogen cycle, C–S isotopic anomalies and deposition of sediments with high organic matter contents (Yan *et al.* 2009; Luo *et al.* 2016; Yan *et al.* 2018).

Neodymium is an essential element for discrimination of source rocks and, thus, plays a major role in analyses of the provenance of sedimentary rocks. Variation of the ^{143}Nd/^{144}Nd in seawater reflects the changes in ocean circulation patterns (Dubois-Dauphin *et al.* 2017), and the isotopic compositions of source rocks. Generally, the source of neodymium mainly contains river water, hydrothermal water and diagenetic waters (Keto & Jacobsen, 1987; Wei *et al.* 2016; Filippova *et al.* 2017). Therefore, marine sedimentary Nd isotopes have been widely used to imply volcanism and tectonism in the source area, and a transportation mechanism of continental and volcanic detritus (Keto & Jacobsen, 1988). Different ^{143}Nd/^{144}Nd ratios in oceanic and continental crust are attributed to fractionation in the process of crustal differentiation, which could produce different Sm/Nd ratios (DePaolo & Wasserburg, 1976). The oceanic crust originating from a depleted mantle shows a higher Sm/Nd ratio and positive εNd(t) value, whereas continental crust, with a low Sm/Nd ratio, shows a negative εNd(t) value (DePaolo & Wasserburg, 1976; Finlay *et al.* 2010; Laukert *et al.* 2017). Hence, the excursion of Nd isotopes could reflect the locally volcanic and tectonic processes. For instance, the dramatic positive excursion of Nd isotopes during ocean anoxic event 2 (OAE2) is interpreted by the emplacement of large igneous provinces (Kenneth *et al.* 2008). Two positive spikes recorded in Nd isotope composition between 20 and 15 Ma were induced by a volcanic crisis (Sandrine *et al.* 2012). It is suggested that the short residence time of Nd in seawater (approximately 300 to 1000 years) relative to the turnover rate of oceans (~1500 years) generally makes Nd isotopes useful proxies to trace water mass origins and ocean circulation patterns (Elderfield, 1988; Tachikawa *et al.* 1999).

The high-resolution Nd isotope evolution during the Ordovician–Silurian transition in the Yangtze Block has been less frequently studied, although some studies have been carried out for the sedimentary Nd isotopic compositions across the O–S transition (Holmden *et al.* 2013). Given this, we carried out a study of geochemical and Nd isotopic characteristics for siliclastic through Late Ordovician to early Silurian. By doing this, we tried to (1) determine the provenance of sediments in the Yangtze Sea; (2) reconstruct the palaeoenvironment in the Yangtze Sea; and (3) discuss the possible links between sea level, redox water conditions and extinctions.

2. Geological setting

During the Late Ordovician interval, South China was located near the equator (Fig. 1a), and was comprised of the Yangtze platform in the NW and the Cathaysia platform in the SE (Yan *et al.* 2015). Subsequently, the Yangtze platform was largely isolated from the open sea as a result of the convergence–compression between the Yangtze Block and Cathaysia Block, as well as the ongoing intracontinental orogeny within the Yangtze Block (Zhang *et al.* 2013). Besides, the Yangtze Sea was divided by the Jiujiang Strait into a western Upper Yangtze Sea and an eastern Lower Yangtze Sea (Chen, 1984). From the Late Ordovician, the Caledonian movement reached its highest intensity, placing the Upper Yangtze Platform under compression and resulting in the formation of Chengdu Uplift in the NW of the Upper Yangtze Platform, Dianqian Uplift in the south of the Upper Yangtze Platform and Jiangnan–Xuefeng Uplift (Fig. 1b) in the SE of the Upper Yangtze Platform (Liang *et al.* 2009; Li *et al.* 2017). Lithofacies and biofacies changes through the O–S transition on the Yangtze platform are coincident with global sea-level changes, and black

shale occupied most of the Yangtze platform region during the late Katian and early Rhuddanian. Black shale was replaced by carbonate facies during the Hirnantian coincident with a global sea-level low stand (Chen *et al.* 2004).

The section analysed in this study is the SC3 core, which was located on the Upper Yangtze platform of the South China Block during the O–S transition; this core was located in a deep shelf facing the open ocean (Fig. 1b). The SC3 profile could be divided into the Wufeng Formation, Guanyinqiao Bed and Lungmachi Formation, in ascending order (Fig. 3, further below). The Wufeng and Lungmachi Formations are mainly composed of black shale with high total organic carbon contents (Fig. 2a), while the Guanyinqiao Bed is composed of carbonaceous mudstones intercalated with carbonaceous limestone bearing abundant benthic fauna (Fig. 2b).

3. Methods

Twenty-six fresh samples of mudstone and calcareous limestone derived from the SC3 core were used for this study, and these samples (200 mesh) were all placed in an oven at 105 °C to dry for 12 hours prior to test.

Preparation for measurement of the $\delta^{13}C_{org}$ involved accurately weighing ~1 g of powdered rock, followed by digestion in HCl to remove carbonate minerals. The residue, including organic matter, silicates and oxides, was thoroughly rinsed, dried and then re-powdered. $\delta^{13}C_{org}$ analyses were performed using a Costech ECS4010 Elemental Analyzer attached to a Thermo Finnigan MAT 253 mass spectrometer (State Key Laboratory of Biogeology and Enviromental Geology, Wuhan). Isotope ratios are reported in delta notation (‰) relative to the Vienna Pee Dee Belemnite (V-PDB) standard (Craig, 1957). The 1σ external precision for $\delta^{13}C_{org}$ is ±e0.1‰ based on repeated analyses of caffeine as an internal standard.

Major element analyses of whole rock were conducted on XRF (X-ray fluorescence) (Primus II, Rigaku, Japan) at the Wuhan Sample solution Analytical Technology Co., Ltd, Wuhan, China. The detailed sample-digesting procedure was as follows: (1) ~1.0 g dried sample was accurately weighed and placed in the ceramic crucible and then heated in a muffle furnace at 1000 °C for 2 hours. After cooling to 400 °C, this sample was placed in the drying vessel and weighed again in order to calculate the loss on ignition (LOI). (2) 0.6 g sample powder was mixed with 6.0 g co-solvent ($Li_2B_4O_7$: $LiBO_2$: LiF = 9:2:1) and 0.3 g oxidant (NH_4NO_3) in a Pt crucible, which was placed in the furnace at 1150 °C for 14 min. This melting sample was then quenched with air for 1 min to produce flat discs on the fire brick for the XRF analyses.

Trace element analysis of whole rock was conducted on Agilent 7700e ICP-MS (inductively coupled plasma mass spectrometer). Firstly, Sample powder (200 mesh) was placed in an oven at 105 °C to dry for 12 hours. For measurement of the trace elements, the bulk sediments were treated using 1 ml HNO_3 and 1 ml HF acid, subsequently drying them twice in an oven at 190 °C. Then the samples were dissolved in 1 ml HNO_3 and spiked with a known amount of Rh. The final solutions were transferred to a polyethylene bottle and diluted to 100 g by the addition of 2 % HNO_3.

Nd isotope analyses were conducted on a Neptune Plus MC-ICP-MS (multi-collector ICP-MS) (Thermo Fisher Scientific, Dreieich, Germany). All chemical preparations were performed on class 100 work benches within a class 1000 over-pressured clean laboratory. Column chemistry: The rare earth elements (REE) solution from the Sr-column method was evaporated to incipient dryness, and taken up with 0.18 M HCl. The converted
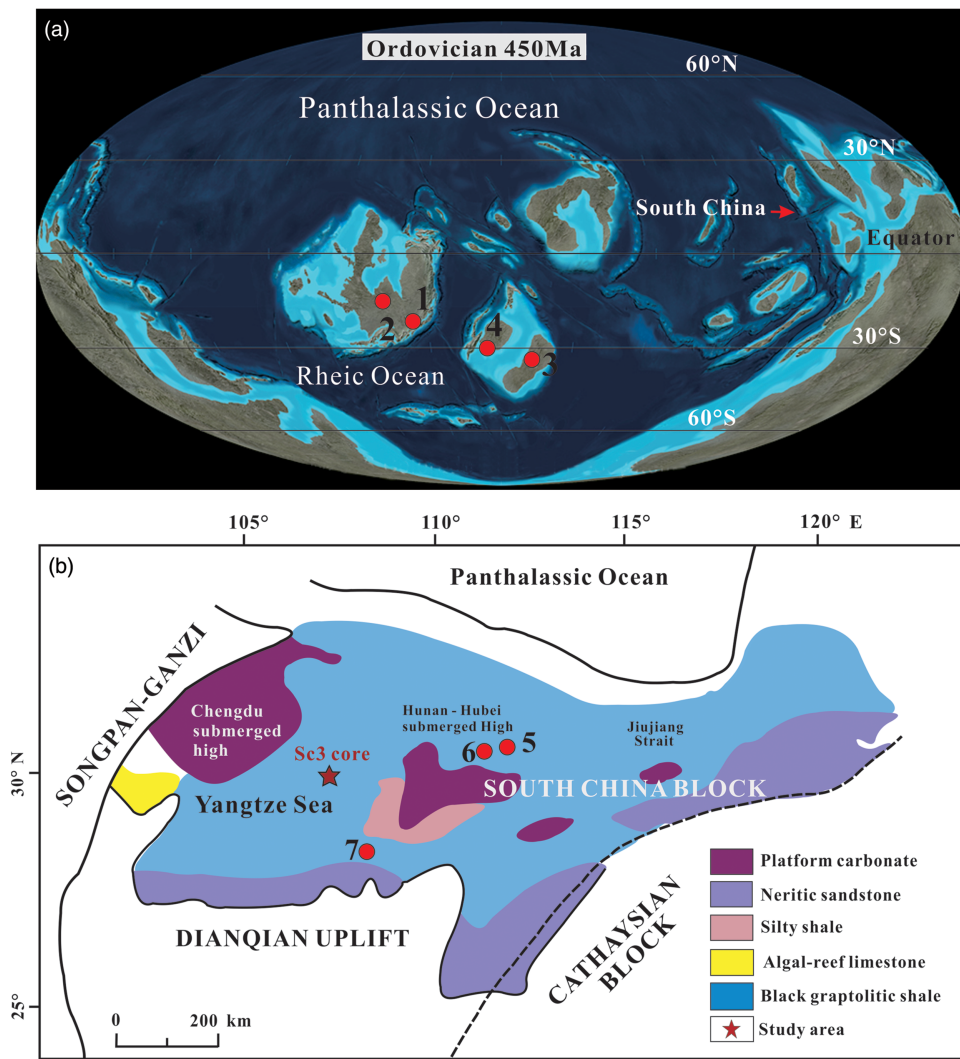
Fig. 1. (Colour online) (a) Palaeogeographic map of the world (the map originates from https://deeptimemaps.com) and (b) Late Ordovician to Early Silurian palaeogeographic map of the Yangtze Block. The relative locations of the Yangtze Block and Cathaysia Block during the O–S transition (modified by Chen *et al.* 2006). 1 – Dob's Linn; 2 – Arctic Canada; 3 – Baltica (Sullivan *et al.* 2018); 4 – Estonia (Young *et al.* 2010); 5 – Wangjiawan (WJW) Section; 6 – Fenxiang (FX) section; 7 – Nanbazi Section.
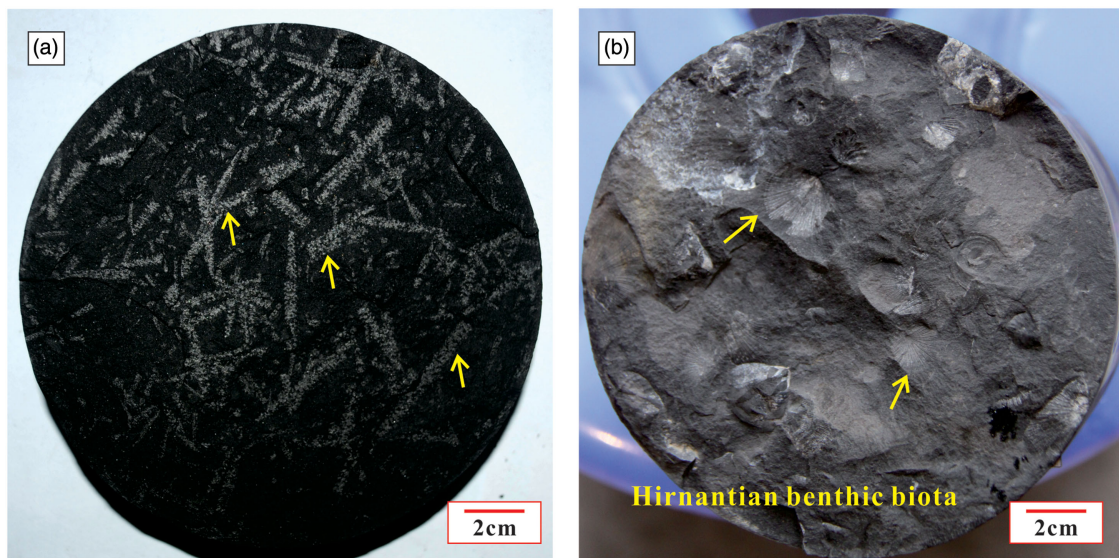
Fig. 2. (Colour online) (a) The black shale in the Wufeng Formation; yellow arrows indicate graptolite. (b) The limestone in the Guanyinqiao Member; large numbers of benthic fauna can be observed.

REE solution was loaded into an anion-exchange column packed with LN resin. After complete draining of the sample solution, columns were rinsed with 0.18 M HCl to remove undesirable matrix elements. Finally, the Sr fraction was eluted using 0.3 M HCl and gently evaporated to dryness prior to mass-spectrometric measurement. In addition, the exponential law, which initially was developed for thermal ionization mass spectrometry (TIMS) measurement (Russell *et al.* 1978) and remains the most widely accepted with MC-ICP-MS, was utilized to assess the instrumental mass discrimination in this study. Mass discrimination correction was performed via internal normalization to a $^{146}Nd/^{144}Nd$ ratio of 0.7219 (Lin et al. 2016). The $\varepsilon Nd(444)$ values were calculated at 444 Ma: $\varepsilon Nd\ (450) = (\{^{143}Nd/^{144}Nd_{sample(0)} - [^{147}Sm/^{144}Nd_{sample(0)}\ (e^{\lambda(450Ma)} - 1)]\}/\{^{143}Nd/^{144}Nd_{CHUR(0)} - [^{147}Sm/^{144}Nd_{CHUR(0)}\ (e^{\lambda(450Ma)} - 1)]\} - 1) \times 10^4$.

4. Results

4.a. Major and trace element geochemistry

The major element concentrations are given in Table 1. The samples from the SC3 core display higher SiO_2 contents (ranging from 13.37 % to 75.13 %), which are regarded as an admixture of three end members: detrital silica, biogenic silica and diagenetic silica (Yang *et al.* 2018). The high Al_2O_3 values (ranging from 3.15 % to 14.42 %) of the samples are mainly related to high clay mineral contents, and the high CaO values (ranging from 1.65 % to 25.99 %) probably indicate calcite enrichment. In the Wufeng and Lungmachi formations, the Ti contents range from 0.43 to 0.54 (average 0.49) and 0.19 to 0.91 (average 0.48) respectively, whereas the Ti contents in the Guanyinqiao Bed display relatively low values, ranging from 0.17 to 0.33 (average 0.26).

The trace element concentrations are given in Table 1. The Zr contents vary from 95.2 to 182.4 ppm (average 137.5 ppm) in the Wufeng Formation, and 60 to 292.1 ppm (average 167.3 ppm) in the Lungmachi Formation. However, the Zr in the Guanyinqiao Bed presents relatively low values, ranging from 61.1 to 117.1 ppm (average 95.2 ppm). Ce anomalies (Ce/Ce*) are traditionally calculated by comparing the normalized concentration of Ce with its neighbouring REE.

4.b. Carbon isotope variations

A $\delta^{13}C_{org}$ profile of the SC3 core was determined for chemostratigraphic correlation of Late Ordovician successions (Fig. 3; Table 2). Our $\delta^{13}C_{org}$ data vary between −31.69 and −28.38 ‰, and the $\delta^{13}C_{org}$ profile shows a positive excursion from about −31.05 ‰ to −28.38 ‰, beginning in the Wufeng Formation (sample 30), with a sharp positive spike up to −28.38 ‰ in the Guanyinqiao Bed (sample 25). A return to pre-excursion values occurs in the Lungmachi Formation (sample 27).

4.c. C_{org}, and P_T compositions

As shown in Table 2, the total organic matter contents (C_{org}) vary generally between 0.09 % and 6.14 % (average 4.08 %), with the lowest abundance in the Guanyinqiao Bed. The total P (P_T) contents vary between 0.06 % and 1.17 % (average 0.18 %), with the highest abundance in the Guanyinqiao Bed.

4.d. Sm–Nd isotope compositions

Nd isotope data for the samples from the SC3 core are reported in Table 3. The Nd and Sm contents of the shale and limestone range

from 11.4 ppm to 76.3 ppm (average 33.8 ppm) and from 2.5 ppm to 16.7 ppm (average 6.7 ppm) in the SC3 core. The $^{143}Sm/^{144}Nd$ and $^{143}Nd/^{144}Nd$ ratios vary from 0.110224 to 0.138411 (average 0.123447) and from 0.511872 to 0.0.512029 (average 0.511940) in the SC3 core. The $\varepsilon Nd(444)$ values for the majority of the Wufeng samples range between −10.28 and −7.87; however, values decrease to −11.14 in the Guanyinqiao Bed. Further upward, the $\varepsilon Nd(444)$ values for the Lungmachi samples return to high values (varying from −9.40 to −8.05).

5. Discussion

5.a. Influence of diagenetic alteration on $\varepsilon Nd(444)$ and Ce/Ce*

The lithofacies assemblage has some differences through the Wufeng Formation to Lungmachi Formation due to the dramatic climatic change during the O–S transition. The Wufeng and Lungmachi formations are mainly characterized by black shale, while the Guanyinqiao Bed is dominated by muddy limestone. It is generally suggested that REE may be mobilized because of diagenetic alteration and thus the sediments could not retain primary geochemical information. The Dy_N/Sm_N ratio is one possible indicator for diagenetic exchange after deposition. It is suggested that the REE patterns would become progressively more Ce-enriched and Dy_N/Sm_N ratios decreased during the diagenetic process (Shields & Stille, 2001; Ling *et al.* 2013). However, there is no apparent correlation between Dy_N/Sm_N vs Ce/Ce*, indicating the diagenetic alteration does not occur in samples from the studied succession (Fig. 3). Furthermore, the Ce anomaly may be influenced by incorporation of Mn oxides that commonly have a positive Ce anomaly, which is due to a lower mobility of Ce^{4+} than REE^{3+}. In our study, the Guanyinqiao limestone with low Ce/Ce* ratios has relatively high Mn contents, suggesting that the effect of Mn oxides on studied samples is limited.

The influence of diagenesis on $\varepsilon Nd(444)$ is due to the preferential loss of light REEs (La–Sm); as a result, this process could significantly alter the Sm/Nd ratio and hence the Nd isotopic compositions (Chakrabarti *et al.* 2007). There is no obvious correlation between Sm/Nd and $\varepsilon Nd(444)$, indicating the diagenetic alteration on studied samples is limited. Another important factor altering the primarily depositional $\varepsilon Nd(444)$ is contamination from continental silicate detritus, because silicate minerals generally have much higher $\varepsilon Nd(444)$ and REE content than carbonate minerals. Such influences from silicate detritus can be monitored by considering the concentrations and correlations of elemental concentrations such as Al of bulk rocks. As shown in Figure 3, a negative relationship between $\varepsilon Nd(444)$ and Al is not observed, suggesting the studied samples are not affected by silicate detritus. In particular, the Guanyinqiao limestone has lower $\varepsilon Nd(444)$ values and Al contents than those in the Wufeng and Lungmachi formations. Therefore, the extremely low $\varepsilon Nd(444)$ values in Guanyinqiao limestone cannot be attributed to the incorporation of silicate detritus; thus, it can reflect the primary ocean signals.

5.b. Constraints on stratigraphic correlation

The Hirnantian stage records a sharp perturbation in the carbon cycle, seen in the enrichment of ^{13}C in both sedimentary carbonate and organic matter; thus, the carbon isotopic chemostratigraphy can serve as a powerful tool for the global correlation. At the SC3 core, $\delta^{13}C_{org}$ data range between −31.69 and −28.38 ‰, and the $\delta^{13}C_{org}$ profile shows a positive excursion from about −31.05 ‰ to −28.38 ‰,

Table 1. Major and trace elements in SC3 core

Samples	KHR-1	KHR-2	KHR-5	KHR-7	KHR-9	KHR-11	KHR-14	KHR-18	KHR-19	KHR-21	KHR-22	KHR-23	KHR-24
Height (m)	5.5	5.8	6.35	6.8	7.3	7.8	8.5	9.7	9.8	10.1	10.4	10.7	10.8
Stratum	Katian	Katian	Katian	Katian	Katian	Katian	Katian	Katian	Katian	Hirnantian	Hirnantian	Hirnantian	Hirnantian
Formation	Wufeng	Wufeng	Wufeng	Wufeng	Wufeng	Wufeng	Wufeng	Wufeng	Wufeng	Wufeng	Wufeng	Wufeng	Guanyinqiao
Lithology	Black shale	Black shale	Black shale	Black shale	Black shale	Black shale	Black shale	Black shale	Black shale	Black shale	Black shale	Black shale	Limestone
TiO_2 (%)	0.46	0.51	0.5	0.52	0.51	0.54	0.54	0.43	0.43	0.48	0.49	0.5	0.29
Al_2O_3 (%)	10.2	10.97	10.67	11.5	10.79	11.45	11.18	8.73	11.51	9.1	9.29	9.24	5.44
P_2O_5 (%)	0.09	0.13	0.11	0.11	0.12	0.12	0.11	0.1	0.12	0.13	0.13	0.12	1.77
MnO (%)	0.02	0.02	0.04	0.02	0.03	0.03	0.03	0.01	0.01	0.02	0.01	0.02	0.17
Zr (ppm)	95.2	116.3	112.2	119.5	133.8	182.4	151.7	130	139.3	151.8	151.5	166.2	117.1
La (ppm)	31.8	38.9	36.2	41	40	47.6	42.6	34.8	33.2	37.6	36.5	33.2	69.2
Ce (ppm)	58.7	73.5	68.1	77.5	75.3	87.6	77.8	65.2	60.8	66.5	69.1	60.3	122.4
Pr (ppm)	6.9	8.7	8	8.8	8.9	10.4	9.2	7.9	7.2	8.1	8.6	7.3	18.2
Nd (ppm)	25.9	33.3	30.5	34.1	34.4	38.8	34.8	29.9	27.8	31.4	32.6	27.7	76.3
Sm (ppm)	4.9	6.4	5.8	6.2	6.6	7.7	6.8	5.9	5.4	6.3	6.7	5.1	16.7
Ti/Al (%/%)	0.045	0.046	0.047	0.045	0.047	0.047	0.048	0.049	0.037	0.053	0.053	0.054	0.052
Zr/Ti (ppm/%)	9.33	10.61	10.51	10.39	12.4	15.92	13.56	14.9	12.11	16.69	16.31	17.98	21.53
GdN/SmN	1.00	1.09	1.12	1.05	1.09	1.11	1.09	1.12	1.15	1.10	1.06	1.07	1.20
Ce/Ce*	0.91	0.92	0.92	0.94	0.92	0.91	0.90	0.91	0.90	0.88	0.90	0.89	0.79
U_{EF}	13.96	16.16	14.67	14.02	19.27	21.24	34.82	41.44	35.67	53.11	28.45	22.87	25.07
Samples	KHR-25	KHR-27	KHR-28	KHR-29	KHR-30	KHR-31	KHR-32	KHR-34	KHR-35	KHR-38	KHR-40	KHR-42	KHR-44
Height	10.9	11	11.1	11.2	11.4	11.6	11.8	12.2	12.4	13	13.7	14.1	14.5
Stratum	Hirnantian	Hirnantian	Hirnantian	Hirnantian	Hirnantian	Rhuddanian	Rhuddanian	Rhuddanian	Rhuddanian	Rhuddanian	Rhuddanian	Rhuddanian	Rhuddanian
Formation	Guanyinqiao	Guanyinqiao	Lumgmachi	Lumgmachi	Lumgmachi	Lumgmachi	Lumgmachi	Lumgmachi	Lumgmachi	Lumgmachi	Lumgmachi	Lumgmachi	Lumgmachi
Lithology	Limestone	Black shale	Black shale	Black shale	Black shale	Black shale	Black shale	Black shale	Black shale	Black shale	Black shale	Black shale	Black shale
TiO_2 (%)	0.17	0.33	0.47	0.37	0.31	0.44	0.19	0.91	0.37	0.43	0.47	0.58	0.7
Al_2O_3 (%)	3.15	5.98	8.4	7.39	5.83	8.08	3.68	10.7	7.57	11.56	10.75	12.43	14.42

(*Continued*)

Samples	KHR-1	KHR-2	KHR-5	KHR-7	KHR-9	KHR-11	KHR-14	KHR-18	KHR-19	KHR-21	KHR-22	KHR-23	KHR-24
P_2O_5 (%)	0.21	0.1	0.14	0.12	0.09	0.12	0.06	0.19	0.09	0.1	0.11	0.08	0.19
MnO (%)	0.47	0.22	0.03	0.03	0.02	0.03	0.02	0.05	0.01	0.02	0.02	0.03	0.03
Zr (ppm)	61.1	107.4	127.6	114.5	106.1	143.1	60	213.4	117.1	173.9	222.2	292.1	270.6
La (ppm)	15.5	27.7	37.3	32	27.9	37.6	17.4	72.5	31.5	42.4	47.4	55.2	69.5
Ce (ppm)	25.8	48.6	70.5	61.6	52.4	69.2	33.1	142	57.5	76.3	84.8	92.2	135.6
Pr (ppm)	3	5.2	8.1	7.2	6.2	8.1	4	16.2	7	9.5	10.4	10.4	16.3
Nd (ppm)	11.4	19.5	30.9	28.2	25	31.5	15.9	61.6	26.7	35.7	39	34.6	61.5
Sm (ppm)	2.5	3.5	6.7	5.6	5.3	6.6	3.2	12.4	5.5	6.8	8.4	6.1	11.4
Ti/Al (%/%)	0.054	0.054	0.056	0.05	0.053	0.054	0.051	0.085	0.048	0.037	0.044	0.047	0.048
Zr/Ti (ppm/%)	19.42	17.96	15.18	15.5	18.21	17.72	16.31	19.95	15.47	15.05	20.66	23.5	18.77
GdN/SmN	1.13	1.18	1.16	1.25	1.24	1.32	1.32	1.18	1.17	1.12	1.14	1.16	0.93
Ce/Ce*	0.86	0.93	0.94	0.94	0.92	0.91	0.92	0.96	0.89	0.88	0.88	0.88	0.93
U_{EF}	4.87	24.39	27.37	38.94	35.13	37.30	26.08	25.29	30.15	15.54	20.94	8.90	5.41

Table 1. (*Continued*)

beginning at the base of the *extraordinarius* zone, and a sharp positive spike up to −28.38 ‰ within the *extraordinarius* zone (Fig. 4). This pattern of $\delta^{13}C_{org}$ is coincident with some sections in other areas, including South China, Baltica, the Arctic and Estonia (Wang, 1989; Melchin & Holmden, 2006; Yan *et al.* 2009; Young *et al.* 2010; Sullivan *et al.* 2018), although some studies also found that the $\delta^{13}C_{org}$ peak should be placed in the lower *persculptus* zone (Underwood *et al.* 1997; Gorjan *et al.* 2012). Furthermore, the $\delta^{13}C_{org}$ return to baseline values in the *persculptus* zone, marking the end of the Hirnantian carbon-isotope excursion (Fig. 4). It seems that there is a step function decrease in $\delta^{13}C_{org}$ whichmay correspond to a sequence-stratigraphic condensation. Condensed sediments are present in mostly well-individualized, extremely thin (<1 m) beds, which were formed over extremely long time periods (>100 ka) (Föllmi, 2016). Interestingly, the time at which $\delta^{13}C_{org}$ decreased was in accord with the characteristics of sequence-stratigraphic condensation. The estimated duration of the *P. persculptus* Biozone was ∼0.6 Ma (Gradstein *et al.* 2012; Chen *et al.* 2015), and the sediments in this interval were constrained in a thin bed (∼0.3m). In addition, the pattern of $\delta^{13}C_{org}$ is consistent with the conclusion, which suggests the elevated $\delta^{13}C_{org}$ in the late *pacificus* – early *extraordinarius* zones and the return to baseline values in the *persculptus* zone appear to be the most significant chemostratigraphic features (Gorjan *et al.* 2012). Overall, the $\delta^{13}C_{org}$ generated in this study is broadly consistent with previously published $\delta^{13}C_{org}$ data, while these new data show a different peak value relative to those at the Wangjiawan, Nanbazi and Fenxiang sections. This excursion is known as the Hirnantian Isotope Carbon Excursion (HICE) (Bergström *et al.* 2008), and matches the timing and magnitude of other known Hirnantian $\delta^{13}C_{org}$ excursions around the world.

5.c. Perturbation in Nd isotopic compositions

The Nd isotopic compositions of whole rock are primarily controlled by the type of source rock transported into the ocean, which generally comprises the oceanic crust originating from a depleted mantle with positive $\varepsilon Nd(t)$ values and the continental crust with negative $\varepsilon Nd(t)$ (DePaolo & Wasserburg, 1976; Keto & Jacobsen, 1988; Wei *et al.* 2016; Filippova *et al.* 2017). High $\varepsilon Nd(t)$ values during the Katian and Rhuddanian intervals can be observed (Fig. 5), and the $\varepsilon Nd(444)$ shift (1.88 unit) occurs during the early Wufeng period. Thus, when considering widely the distribution of K-bentonite in South China, this high $\varepsilon Nd(444)$ value may indicate the high radioactive ^{143}Nd flux provided by volcanic activities. This phenomenon is in accordance with previous studies, in which the largest positive $\varepsilon Nd(t)$ excursion during OAE2 was due to the eruptions of the Caribbean large igneous province (Kenneth *et al.* 2008).

The $\varepsilon Nd(t)$ values decrease sharply at the base of the glaciation period, and then remain low and relatively constant before an abrupt return to high values (Fig. 5). Possible explanations for the low values include (1) a diagenetic overprint, (2) change in the source rocks, (3) sinking of a locally derived water mass imprinted with an $\varepsilon Nd(t)$ value strongly impacted by continental weathering, or (4) seawater–particle exchange coupled with generally sluggish circulation (Kenneth *et al.* 2008). The alteration by diagenesis is excluded in section 5.a, especially as, if the Nd isotopic excursion is a diagenetic artefact, it will be expected to occur at a lithologic transition, resulting from the diagenesis generally exerting similar influences on the same rock types. However, Nd isotope actually shifts within the black shale unit (Fig. 5),
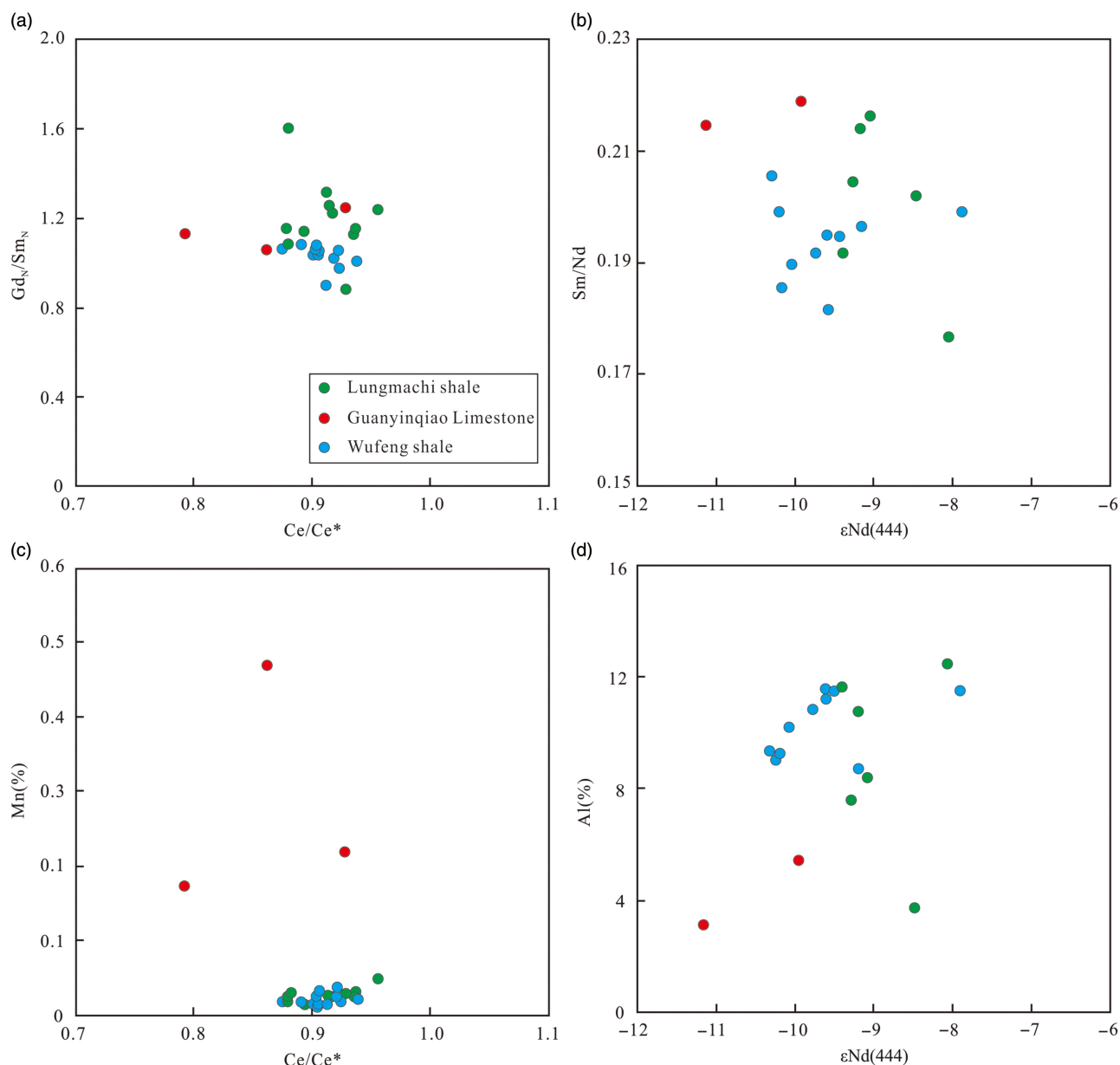
Fig. 3. (Colour online) (a) Plot of Ce/Ce* vs Gd_N/Sm_N ratios. (b) Plot of $\varepsilon Nd(444)$ vs Sm/Nd ratios. (c) Plot of Ce/Ce* vs Mn contents. (d) Plot of $\varepsilon Nd(444)$ vs Al contents.

thereby indicating that diagenetic effect is not the major factor controlling the variation of $\varepsilon Nd(444)$.

There are a number of ways of inferring the provenance composition from the chemical composition of finer siliciclastics (Cullers & Podkovyrov, 2000), resulting from the fact that the immobile major and trace elements (e.g. Zr, REE, high-field strength elements (HFSE)) in siliciclastic rocks are particularly sensitive to provenance. Being immobile in natural sedimentary environments, Al_2O_3, TiO_2, Th and Zr, and other HFSEs are quantitatively transferred as detrital load from the source rocks (Taylor & McLennan, 1985; Hayashi *et al.* 1997). Hayashi *et al.* (1997) observed that mafic igneous rocks are characterized by a TiO_2/Zr weight ratio of >195, intermediate igneous rocks by a ratio of between 195 and 55, and felsic igneous rocks by one of <55. They proposed a scheme for discriminating the source of the sedimentary rocks on the basis of TiO_2/Zr weight ratios. As presented in this discriminating scheme, the TiO_2/Zr weight ratios of studied

samples indicate felsic igneous source rock (Fig. 6a). The Al_2O_3/TiO_2 ratio is another important indicator for the provenance composition (Hayashi *et al.* 1997). The Al_2O_3/TiO_2 ratios of SC3 black shales range between 12 and 27, suggesting their derivation from felsic igneous source rocks. The plots of black shale samples in the Al_2O_3–TiO_2 bivariate space (Fig. 6b; McLennan *et al.* 1979; Schieber, 1992) clearly suggest granodiorite source rock for SC3 black shales; thus, the Nd isotopic excursion is not controlled by the difference in source rocks.

Instead, abrupt eustatic fall is likely to be the reason for this Nd isotopic excursion. It has been proposed that the Nd isotopes can be invoked as a sea-level proxy from the western margin of Laurentia during the O–S transition. Furthermore, when sea level was high and palaeo – shorelines had migrated eastward, the $\varepsilon Nd(t)$ value of seawater shifted toward the $\varepsilon Nd(t)$ value of the eastern Panthalassa Ocean ($\sim$−4.0), whereas the $\varepsilon Nd(t)$ of seawater shifted toward the $\varepsilon Nd(t)$ value of the continental

Table 2. C- and P-compositions of studied sediments

Samples	Stratum	Formation	Lithology	$\delta^{13}C_{org}$ (‰)	C_{org} (%)	C_{org}/P_T (mol/mol)	C_{org} (mol)	P_T (mol)
KHR-2	Katian	Wufeng	Black shale	−30.94	4.74	94.87	0.39	0.0042
KHR-5	Katian	Wufeng	Black shale	−30.85	3.86	90.6	0.32	0.0035
KHR-7	Katian	Wufeng	Black shale	−30.98	3.92	96.46	0.33	0.0034
KHR-8	Katian	Wufeng	Black shale	−31.07	n.d.	n.d.	n.d.	n.d.
KHR-9	Katian	Wufeng	Black shale	−30.76	4.58	101.98	0.38	0.0037
KHR-11	Katian	Wufeng	Black shale	−30.91	4.33	93.18	0.36	0.0039
KHR-12	Katian	Wufeng	Black shale	−30.93	n.d.	n.d.	n.d.	n.d.
KHR-14	Katian	Wufeng	Black shale	−31.24	4.8	108.76	0.4	0.0037
KHR-15	Katian	Wufeng	Black shale	−31.08	n.d.	n.d.	n.d.	n.d.
KHR-16	Katian	Wufeng	Black shale	−30.33	n.d.	n.d.	n.d.	n.d.
KHR-18	Katian	Wufeng	Black shale	−30.85	4.6	116.41	0.38	0.0033
KHR-19	Katian	Wufeng	Black shale	n.d.	6.14	130.05	0.51	0.0039
KHR-20	Katian	Wufeng	Black shale	−31.05	n.d.	n.d.	n.d.	n.d.
KHR-21	Hirnantian	Wufeng	Black shale	−30.35	3.93	78.15	0.33	0.0042
KHR-22	Hirnantian	Wufeng	Black shale	−30.62	4.56	87.88	0.38	0.0043
KHR-23	Hirnantian	Wufeng	Black shale	−30.57	3.94	88.56	0.33	0.0037
KHR-24	Hirnantian	Guanyinqiao	Limestone	−29.41	2.4	3.49	0.2	0.0572
KHR-25	Hirnantian	Guanyinqiao	Limestone	−28.38	0.36	4.46	0.03	0.0066
KHR-27	Hirnantian	Guanyinqiao	Limestone	−30.63	0.09	2.34	0.01	0.0034
KHR-28	Hirnantian	Lumgmachi	Black shale	−31.26	3.15	57.33	0.26	0.0046
KHR-29	Hirnantian	Lumgmachi	Black shale	−31.21	4.81	107.1	0.4	0.0037
KHR-30	Hirnantian	Lumgmachi	Black shale	−31.59	3.67	106.62	0.31	0.0029
KHR-31	Rhuddanian	Lumgmachi	Black shale	−31.43	5.18	114.34	0.43	0.0038
KHR-32	Rhuddanian	Lumgmachi	Black shale	−31.41	n.d.	n.d.	n.d.	n.d.
KHR-33	Rhuddanian	Lumgmachi	Black shale	−31.69	n.d.	n.d.	n.d.	n.d.
KHR-34	Rhuddanian	Lumgmachi	Black shale	−31.49	5.15	69.3	0.43	0.0062
KHR-35	Rhuddanian	Lumgmachi	Black shale	−31.26	5.93	164.84	0.49	0.0030
KHR-36	Rhuddanian	Lumgmachi	Black shale	−31.53	n.d.	n.d.	n.d.	n.d.
KHR-37	Rhuddanian	Lumgmachi	Black shale	−31.41	n.d.	n.d.	n.d.	n.d.
KHR-38	Rhuddanian	Lumgmachi	Black shale	−30.89	4.57	114.57	0.38	0.0033
KHR-41	Rhuddanian	Lumgmachi	Black shale	−30.74	n.d.	n.d.	n.d.	n.d.
KHR-42	Rhuddanian	Lumgmachi	Black shale	−30.68	4.04	125.9	0.34	0.0027
KHR-44	Rhuddanian	Lumgmachi	Black shale	−30.71	n.d.	n.d.	n.d.	n.d.
KHR-45	Rhuddanian	Lumgmachi	Black shale	−30.84	n.d.	n.d.	n.d.	n.d.

n.d.: no data.

weathering flux from Laurentia (∼−8.5) when sea level was low (Holmden *et al.* 2013). During the O–S interval, the Upper Yangtze Basin was surrounded by a series of uplifts and oldlands, such as the Xuefeng, Qianzhong and Chuanzhong uplifts and the Hanzhong and Kangdian oldlands (Fig. 1). Additionally, there are many temporary submarine highs including the Chengdu, Hunan–Hubei, Dongting and Poyang. These submarine highs were defined to indicate the area with big gaps from the Lower Cambrian to Lower Silurian. Sediments in the Yangtze Sea were mainly transported from continent to basin depending on the river during that time, ultimately forming the mudstone and limestone within the Yangtze Sea. Importantly, the sea-level fall during glaciation would lead to exposure of the submarine highs and growth of the Yangtze Oldlands, making for more continental materials (low $\varepsilon Nd(t)$ values) poured into the Yangtze Sea.

Yan *et al.* (2010) used the chemical index of alteration (CIA) as a proxy for changes in intensity of chemical weathering, and they suggested that the Katian and Rhuddanian periods were characterized by intense chemical weathering. In contrast, the early Hirnantian was characterized by weak chemical weathering as a result of cold and arid climate. This result is not consistent with the $\varepsilon Nd(t)$ variation, due to the fact that the products

Table 3. Sm–Nd isotope compositions of studied samples

Samples	Stratum	Formation	Lithology	Sm/Nd	$^{143}Nd/^{144}Nd$	2σ (× 10^{-6})	$^{143}Sm/^{144}Nd$	$\varepsilon Nd\,(t)$
KHR-1	Katian	Wufeng	Black shale	0.18949502	0.511900	6	0.119836	−10.05
KHR-7	Katian	Wufeng	Black shale	0.18155776	0.511896	4	0.110224	−9.58
KHR-9	Katian	Wufeng	Black shale	0.19173913	0.511905	4	0.116405	−9.75
KHR-11	Katian	Wufeng	Black shale	0.19898988	0.512029	5	0.125840	−7.87
KHR-14	Katian	Wufeng	Black shale	0.19477759	0.511919	4	0.118250	−9.59
KHR-18	Katian	Wufeng	Black shale	0.19648864	0.511957	5	0.124259	−9.18
KHR-19	Katian	Wufeng	Black shale	0.19461698	0.511925	5	0.118152	−9.46
KHR-21	Hirnantian	Wufeng	Black shale	0.19932343	0.511895	4	0.121009	−10.21
KHR-22	Hirnantian	Wufeng	Black shale	0.20541697	0.511917	8	0.129905	−10.28
KHR-23	Hirnantian	Wufeng	Black shale	0.18517547	0.511872	5	0.112420	−10.17
KHR-24	Hirnantian	Guanyinqiao	Limestone	0.21886814	0.511960	4	0.138411	−9.92
KHR-25	Hirnantian	Guanyinqiao	Limestone	0.2145576	0.511890	2	0.135685	−11.14
KHR-28	Hirnantian	Lumgmachi	Black shale	0.21613253	0.512000	6	0.136681	−9.05
KHR-32	Rhuddanian	Lumgmachi	Black shale	0.20168423	0.511989	7	0.122443	−8.46
KHR-35	Rhuddanian	Lumgmachi	Black shale	0.20432439	0.511967	5	0.129214	−9.26
KHR-38	Rhuddanian	Lumgmachi	Black shale	0.19158056	0.511923	5	0.116309	−9.40
KHR-40	Rhuddanian	Lumgmachi	Black shale	0.2139121	0.511990	5	0.135277	−9.17
KHR-42	Rhuddanian	Lumgmachi	Black shale	0.1766633	0.511979	4	0.111721	−8.05
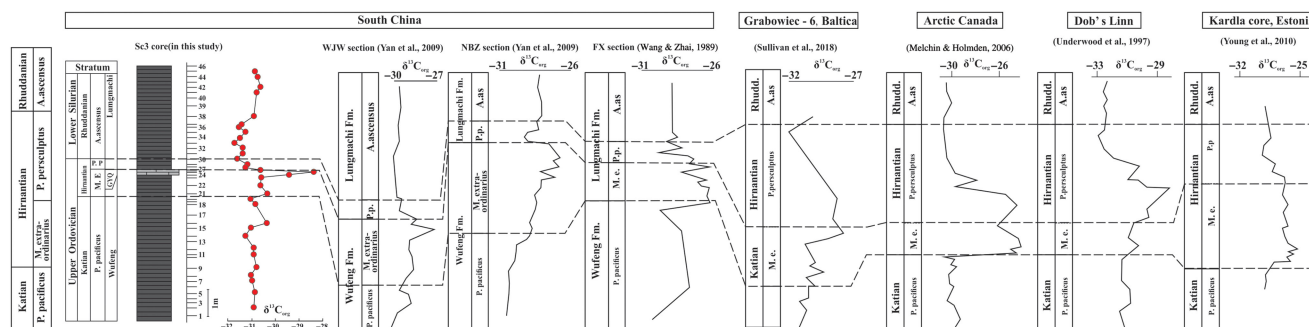
Fig. 4. (Colour online) Carbon isotopic variations across the O–S transition at SC3 (in this study), Wangjiawan (WJW), Nanbazi (NBZ), Fenxiang (FX) in South China (Wang, 1989; Yan *et al.* 2009), and their correlation with those at Baltica (Sullivan *et al.* 2018), Arctic Canada (Melchin & Holmden, 2006), Dob' Linn (Underwood *et al.* 1997) and Estonia (Young *et al.* 2010). The locations of the sections are shown in Figure 1. Biostratigraphy based on Chen *et al.* (2015, 2017). M. e: *M. extraordinarius*; P.p: *P. persculptus*; A. as: *A. ascensus*.

transported into Yangtze Sea were sourced from not only chemical weathering but also physical weathering. Zr and Ti concentrations are generally considered as indicators of detrital flux because these elements are linked to heavy minerals and clay minerals. The Ti/Al and Zr/Al display relatively consistent values between 0.037 and 0.045, and between 9.33 and 15.92. However, the increase in Ti/Al and Zr/Al ratios occurs at the base of Hirnantian, which is coincident with the positive $\varepsilon Nd(t)$ shift. Likewise, the time at which $\varepsilon Nd(t)$ decreased also coincides with that for Ti/Al and Zr/Al ratios, indicating the strong relationship between high terrestrial input and low $\varepsilon Nd(t)$ values. Therefore, we propose that high $\varepsilon Nd(t)$ values in the Katian, late Hirnantian and Rhuddanian were associated with low terrestrial input, whereas the low sea level during the early Hirnantian period resulted in high terrestrial input and low $\varepsilon Nd(t)$ values.

It is worth noting that the negative $\varepsilon Nd(t)$ values may also be related to the formation of an isolated Yangtze Sea when sea level was low. The Panthalassa Ocean in the Late Ordovician was, like today's Pacific Ocean, strongly influenced by inputs of Nd from island arc weathering (Keto & Jacobsen, 1988; Holmden *et al.* 2013). In this case, weak circulation between the Yangtze Sea and Panthalassa Ocean could lead to less material with high $\varepsilon Nd(t)$ values being transported into the Yangtze Sea.

The εNd profiles for the two platform sections yielded similar proxy sea-level curves with several cycles of oscillation recorded during the Hirnantian period (Fig. 7; Holmden *et al.* 2013). Such εNd data support previous findings that the Hirnantian ice age comprised two major glacial periods separated by a minor interglacial during the early part of the *Metabolograptus persculptus* Biozone. The younger glacial (confined to mid *M. persculptus* Biozone time) led to more extensive sea surface cooling than did the earlier one, and resulted in extensive eustatic sea-level draw-down and C-cycle changes. In our study, it seems that the high εNd values during the Hirnantian glaciation could be divided into

Fig. 5. (Colour online) The stratigraphic distribution of the $\delta^{13}C_{org}$, $\varepsilon Nd(444)$, terrestrial input and redox proxies.

Fig. 6. (Colour online) (a) TiO_2–Zr discrimination plots indicating felsic igneous source rocks for the SC3 shales. TiO_2–Zr discriminating field values are after Hayashi *et al.* (1997). (b) Al_2O_3–TiO_2 bivariate space (after McLennan *et al.* 1979) suggesting granite–granodiorite source rock for the SC3 shales. The 'granite line' and the '3 granite + 1 basalt line' are from Schieber (1992). Post-Archaean average Australian shale (PAAS; Taylor & McLennan, 1985) is also plotted for reference. Plots of granodiorite, gabbro, peridotite and alkali granite are after Paikaray *et al.* (2008).

two stages. The εNd has relatively uniform values in the first stage and is constrained within the *Metabolograptus extraordinarius* Biozone. However, the εNd clearly increased during the early *M. persculptus* Biozone, which may indicate the younger glacial. Overall, the εNd data correlate well with the assumption concluded above.

During the O–S transition in the western margin of Laurentia, the variation of εNd (from −4 to −8) recorded several cycles of oscillation (Holmden *et al.* 2013), while the Yangtze Sea maintained relatively constant εNd values (varying from −10 to −11) prior to the Hirnantian. The differences in variation of εNd between these two areas can be attributed to three aspects: (1) The short residence time of Nd in seawater (approximately 300 to 1000 years) relative to the turnover rate of the oceans (~1500 years) generally makes Nd isotopes useful proxies to reflect regional basin, rather than the global, change in water mass. Thus, it is possible that the Yangtze area and the western margin of Laurentia are characterized by different εNd profiles. (2) The Middle Palaeozoic event is widely recognized in the South China Craton, which is identified as the angular and parallel unconformity between Devonian and Pre-Devonian strata. The influence of the Kwangsian Orogeny varies across the South China Craton, and this event migrated through SE to NW on the basis of biostratigraphic and lithostratigraphic analysis

(Chen *et al.* 2012). Several studies have demonstrated that the change from carbonate to shale and siliciclastic sediments in the Yangtze area is caused by basement subsidence and sea–level rise (Chen *et al.* 2004; Ma *et al.* 2009). Thus, the sea-level variability in the Yangtze Sea is controlled by both local tectonism and global climatic change. (3) The lithologies studied here are dominated by shale and muddy limestone that differ in some important ways from those reported by Holmden *et al.* (2013). Due to the different sedimentation rate between the western margin of Laurentia and the Yangtze Sea, the thicknesses of Hirnantian sediments in the Monitor Range, Vinini Creek and Blackstone River sections are ~80 m, 12 m and 20 m respectively, all of which are much thicker than in the studied section (~1 m).

The degree of weathering is of great significance to the environmental and biological evolution (Finlay *et al.* 2010; Yan *et al.* 2010). Interestingly, the change in Nd isotopic compositions can reflect the terrestrial influx and the degree of physical weathering, thereby not only influencing the sedimentary rate, but also controlling the transporting efficiency of nutritive elements that are indispensable to marine biology. The Nd isotopic composition demonstrated that the Hirnantian interval has exhibited obviously elevated physical weathering, which is consistent with the claim according to global Sr isotopic composition (Hu *et al.* 2017). However, it
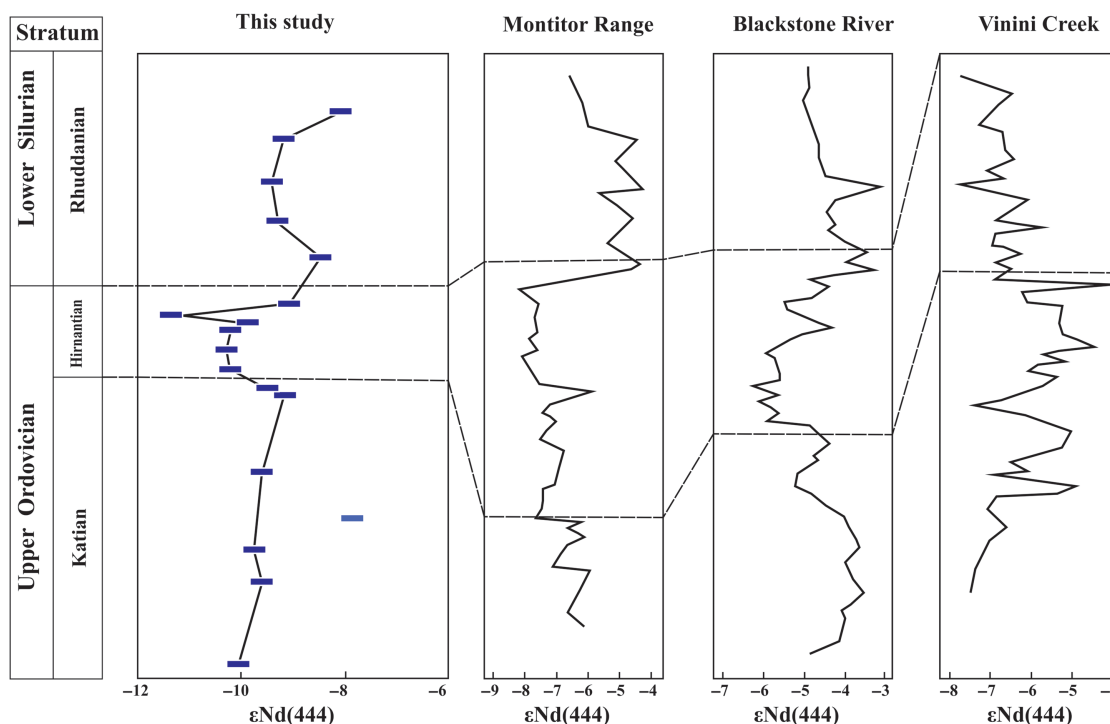
Fig. 7. (Colour online) General trends of the Nd isotopic composition in South China (this study) and western margin of Laurentia respectively (Holmden *et al.* 2013).

contradicts previous opinion that the Hirnantian glaciation was characterized by weak chemical weathering based on Os isotopic composition and the CIA (Finlay *et al.* 2010; Yan *et al.* 2010). The interplay between physical and chemical erosion over glacial–interglacial cycles has been evaluated by Schachtman *et al.* (2019). They observed low CDF values (<0.1) and rapid denudation (>0.22 mm a^{-1}) during the cold and sparsely forested Last Glacial (LG) (29–14 ka). So far, few studies have attempted to estimate how these two processes each influence the climate, and more such studies are needed in the future.

5.d. The redox water conditions

Previous studies have confirmed that the oceanic environment patently changed during the O–S transition. In order to explore the redox conditions in the Yangtze Sea across the O–S transition, multiple palaeoredox proxies were used, including S/C, Fe_{HR}/Fe_{T}, Fe_{P}/Fe_{HR}, DOP values, $\delta^{34}S$ and $\delta^{98}Mo$ values. The results indicate a predominance of stratified, anoxic (ferruginous) ocean on the Yangtze block during this interval, which was interrupted by a brief episode of oceanic oxygenation in the early Hirnantian. This oxygenation, temporally coinciding with the end-Ordovician glaciation and global eustatic sea-level fall, likely resulted from enhanced circulation of polar cold, dense oxygen-rich water onto the low-latitude shelf (Yan *et al.* 2012; Zhou *et al.* 2015).

Observations of total organic carbon contents, combined with descriptions of sedimentary structure (laminated or bioturbated) and benthic faunal abundance, could qualitatively evaluate the sea-floor oxygenation (Arthur & Sageman, 1994). The Wufeng and Lungmachi formations in the SC3 core are dominated by black, laminated fabric, organic-rich shale and mudstone (Fig. 2a). Generally, these organic-rich shales were deposited under relatively anoxic water conditions. In contrast, the Guanyiniqiao Bed is characterized by grey, organic-poor argillaceous limestone

(Fig. 2b). In addition, abundant benthic fauna can be observed, suggesting that the Guanyinqiao sediments are likely to have been deposited under oxic water conditions.

The U and Mo are considered to be effective indicators for redox water conditions because they are sensitive to changes in variation of oxygen in the water column (Algeo & Tribovillard, 2009). It is generally accepted that the enrichment factors could reflect the redox water conditions according to the geochemical behaviour of U. Based on previous studies, the enrichment factor of U was calculated as: $U_{EF} = [(U/Al)_{sample}/(U/Al)_{PAAS}]$, where U and Al represent the weight per cent concentrations of elements U and Al respectively, and PAAS represents post-Archaean average shale compositions (Taylor & McLennan, 1985). This study calculates the enrichment factor of U (U_{EF}), and the result shows that U_{EF} values range from 4.87 to 53.11 in the SC3 borehole. The U_{EF} value gradually ascended throughout the Katian period, and then displayed a sharp decrease at the base of the Hirnantian stage (Fig. 5). Subsequently, U_{EF} maintained uniform and high values during the late Hirnantian and Rhuddanian intervals. This variation trend is in good correlation with the change in lithofacies assemblage, suggesting that the Yangtze Sea gradually became oxygen-rich through the Wufeng to Guanyinqiao period.

Negative Ce anomalies are ubiquitous in the modern, well-oxygenated ocean, but their magnitude varies within and between ocean basins (De Baar *et al.* 1985; De Baar 1991), and can respond to changes in water column redox on a metre scale (e.g. De Carlo & Green, 2002). As a consequence, Ce anomaly is considered an important redox indicator for the sedimentary environment of shale and limestone (Elderfield & Greaves, 1982; Wright *et al.* 1987; German & Elderfield, 1990; Murry *et al.* 1992). In modern stratified water columns, negative Ce anomalies develop in the oxic surface waters and are eroded in intermediate conditions, with Ce anomalies absent in deeper fully anoxic waters (German *et al.* 1991). For instance, the depth profile of Ce anomaly of the Black Sea shows values of 0.1 in oxidizing surface water and 1.0 in

sulphide-precipitating anoxic bottom water (German et al. 1991). Debaar et al. (1988) found that the present-day profile of Ce anomaly in the Cariaco displayed a very sharp decrease at the oxic–anoxic boundary near 300 m. Overall, the magnitude of the negative Ce anomaly in marine sediments is related to redox water conditions. Secular variation of whole-rock Ce anomalies in the SC3 core fluctuates between 0.79 and 0.96 during the O–S transition, and a remarkable stratigraphic change of Ce anomaly is recognized in the early Hirnantian stage (Fig. 5). The Ce negative anomaly of the time sequence of the Late Ordovician to Early Silurian provides evidence for the development of a largely stagnant stratified ocean with anoxic bottom water, which presumably began to form in the Upper Ordovician and persisted into the Lower Silurian, and for a temporary oxic at the early Hirnantian interval.

P is an important redox-sensitive element, and it is, to a great extent, controlled by the bottom-water redox conditions (Froelich et al. 1979; Bostrom et al. 1988; McManus et al. 1997; Filippelli, 2002; Algeo & Ingall, 2007). Under oxic–suboxic water column conditions, much of the P derived from organic matter decomposition may remain in sediments as a result of adsorption and complexation reactions, as well as storage of polyphosphates by microorganisms. Therefore, the oxic–suboxic conditions are more favourable for P preservation but unfavourable for organic C (C_{org}) preservation, resulting in the low C_{org}/P_T ratios in sediments. However, the reductive dissolution of Fe oxyhydroxides allows most of the associated P to diffuse out of the sediment, which does not favour preservation of P and results in high C_{org}/P_T ratios (Algeo & Ingall, 2007). In this case, the C_{org}/P_T ratio of bulk sediment can be used as a reliable proxy for redox water conditions (Sageman et al. 2003; Algeo & Ingall, 2007). Previous studies summarized the C_{org}/P_T in modern marine sediments and their relationship to bottom-water redox conditions (Algeo & Ingall, 2007). It is proposed that the anoxic environments are characterized by the highest C_{org}/P_T ratios (~150 to ~200); intermediate median C_{org}/P_T ratios are exhibited by suboxic environments (~75 to ~130); and the oxic water conditions are dominated by the lowest C_{org}/P_T ratios (<~40). Based on the organic C and total P concentration data, the studied samples display relatively high C_{org}/P_T ratios in both the Katian and Rhuddanian intervals, ranging from 90 to 130 and from 69 to 164, indicating an anoxic water condition, whereas, the samples from the early Hirnantian are characterized by lower C_{org}/P_T ratios relative to those from Katian and Rhuddanian, suggesting a relatively oxic water condition (Fig. 5).

In summary, the present data provides strong evidence for change in the depositional environment. During the Katian, late Hirnantian and Rhuddanian intervals, the stagnant seawaters in the Yangtze Sea might have been caused by the high sea level, while the drop in sea level during the early Hirnantian could have enhanced the circulation of dense oxygen-rich waters onto the floor of the Yangtze Sea, leading to sediments being deposited under oxic water conditions.

5.e. Implications for the causes of the Late Ordovician Extinction

The Late Ordovician biotic crisis was marked by two-phase extinction events, and a variety of kill mechanisms have been put forward, mostly invoking global ocean temperature, volcanism, euxinia and changes in redox chemistry (Yan et al. 2010; Hammarlund et al. 2012; Zhou et al. 2015; Jones et al. 2017). During the Katian period, the Yangtze Sea was characterized by high sea level, anoxic water conditions and low terrestrial
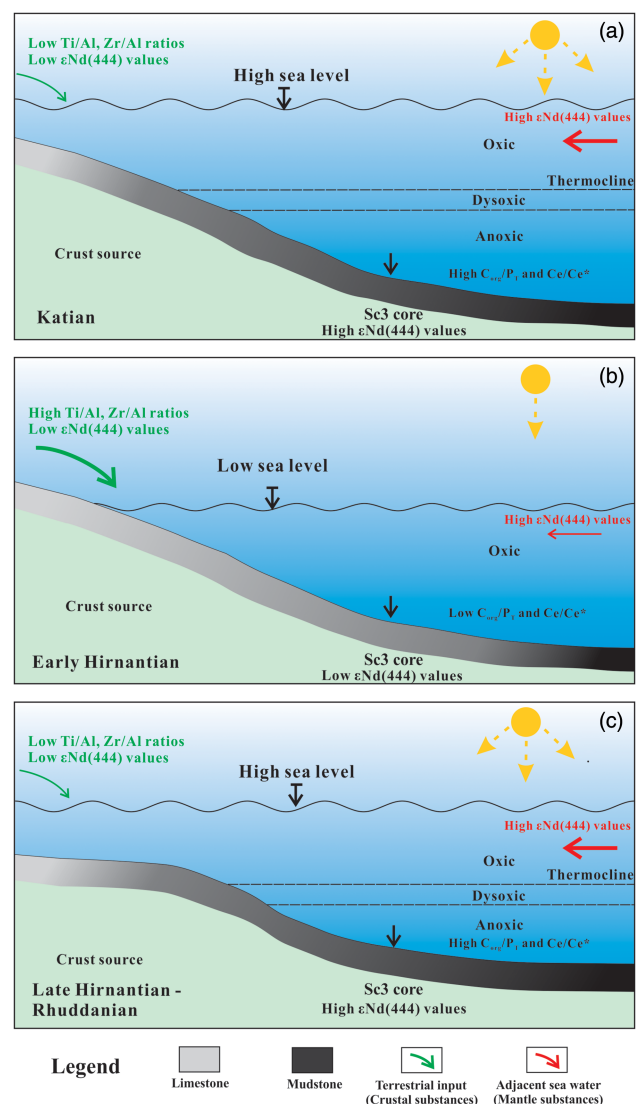
Fig. 8. (Colour online) A model for the deposition of sediments during the O–S transition: (a) during the Katian interval; (b) during the Early Hirnantian interval; (c) during the late Hirnantian and Rhuddanian intervals.

input (Fig. 8a). The first strike occurred in the beginning of the Hirnantian, coincident with the rapid sea-level fall (Fig. 8b), which seriously damaged marine ecosystems and reduced biodiversity. This sea-level fall resulted in the loss of large areas of shallow marine habitat; in particular, it is regarded as the principal cause of the first phase of benthic extinctions (e.g. Berry & Boucot, 1973; Owen & Robertson, 1995; Elias & Young, 1998). In the meantime, the large-scale sea-level fall caused by the Hirnantian Glaciation could have resulted in the environmental changes from anoxic to oxygenated bottom waters. In this case, increased oxygenation might have reduced habitat for one of the primary victims, the graptolites, which are considered to be eutrophic, dysoxic deep-water dwellers (Wilde & Berry, 1984; Cooper et al. 2012; Melchin et al. 2013). Regarding the second extinction interval in the late Hirnantian stage, which is consistent with the rapid sea-level rise, the shift from oxygenated to anoxic marine waters could have exerted severe ecological stresses on victims that had been adapted to oxygenated conditions. During the late Hirnantian and Rhuddanian intervals, the Yangtze Sea was characterized by high sea level, anoxic water conditions and low terrestrial input (Fig. 8c).

6. Conclusions

The geochemical data provide a record of changing environmental conditions associated with the Hirnantian Glaciation in the Yangtze area, from which we draw the following conclusions:

(1) The Nd isotopic compositions in the Yangtze Sea are a combination of two sources: the continental erosion and the Panthalassa Ocean. High εNd(t) values during the Katian, late Hirnantian and Rhuddanian intervals are associated with high sea level, which resulted in less terrestrial input based on low Ti/Al and Zr/Al ratios. In contrast, low εNd(t) values during the early Hirnantian interval are related to sea-level fall. In this case, the exposure of submarine highs and the growth of Yangtze Oldlands lead to more continental materials being transported into the Yangtze Sea based on high Ti/Al and Zr/Al ratios. Additionally, the negative εNd(t) excursion during the O–S transition can also be attributed to the weak circulation between the Yangtze Sea and Panthalassa Ocean when sea-level was low.

(2) The sea-level fluctuations play a significant role in the change in redox water conditions. During the Katian and Rhuddanian intervals, high Ce/Ce* and C_{org}/P ratios suggest that the Yangtze Sea was characterized by anoxic water conditions caused by high sea level, while the drop in sea level during the early Hirnantian could enhance circulation of dense oxygen-rich waters onto the floor of the Yangtze Sea. Thus, the sediments were deposited under oxic water conditions based on relatively low Ce/Ce*, U_{EF} and C_{org}/P values.

(3) The Late Ordovician biotic crisis was marked by two-phase extinction events, and the change in sea level and redox chemistry may be the important kill mechanisms.

References

Algeo TJ and Ingall E (2007) Sedimentary C_{org}:P ratios, paleocean ventilation, and Phanerozoic atmospheric pO_2. *Palaeogeography, Palaeoclimatology, Palaeoecology* **256**, 130–55.

Algeo TJ, Marenco PJ and Saltzman MR (2016) Co-evolution of oceans, climate, and the biosphere during the 'Ordovician Revolution': a review. *Palaeogeography, Palaeoclimatology, Palaeoecology* **458**, 1–11.

Algeo TJ and Tribovillard N (2009) Environmental analysis of paleoceanographic systems based on molybdenum–uranium covariation. *Chemical Geology* **268**, 211–25.

Arthur MA and Sageman BB (1994) Marine black shales: depositional mechanisms and environments of ancient deposits. *Annual Review of Earth and Planetary Sciences* **22**, 499–551.

Bergström SM, Chen X and Gutierrez JC (2008) The new Chronostratigraphic classification of the Ordovician System and its relations to major regional series and stages and to δ^{13}C chemostratigraphy. *Lethaia* **42**, 97–107.

Berry WBN and Boucot AJ (1973) Glacio-eustatic control of Late Ordovician–Early Silurian platform sedimentation and faunal changes. *Geological Society of America Bulletin* **84**, 275–84.

Bostrom M, Andersen S and Fleischer S (1988) Exchange of phosphorus across the sediment-water interface. *Hydrobiologia* **170**, 229–44.

Brenchley PJ, Carden GAF and Hint L (2003) High-resolution stable isotope stratigraphy of Upper Ordovician sequences: constraints on the timing of bioevents and environmental changes associated with mass extinction and glaciation. *Geological Society of America Bulletin* **115**, 89–104.

Chakrabarti R, Abanda P and Hannigan R (2007) Effects of diagenesis on the Nd-isotopic composition of black shales from the 420 Ma Utica Shale Magnafacies. *Chemical Geology* **244**, 221–31.

Chen X (1984) Influence of the Late Ordovician glaciation on the basin configuration of the Yangtze Platform in China. *Lethaia* **17**, 51–9. doi: 10.1111/j.1502-3931.1984.tb00665.x.

Chen X, Fan JX and Wang WH (2017) Stage-progressive distribution pattern of the Lungmachi black graptolitic shales from Guizhou to Chongqing, Central China. *Science China Earth Sciences* **60**, 1133–46. doi: 10.1007/s11430-016-9031-9

Chen X, Fan JX and Zhang YD (2015) Subdivision and delineation of the Wufeng and Lungmachi black shales in the subsurface areas of the Yangtze Platform. *Journal of Stratigraphy* **39**, 351–8.

Chen X, Rong JY and Fan JX (2006) The Global Boundary Stratotype Section and Point (GSSP) for the base of the Hirnantian stage (the uppermost of the Ordovician System). *Episodes* **29**, 183–96.

Chen X, Rong JY and Li Y (2004) Facies patterns and geography of the Yangtze region, South China, through the Ordovician and Silurian transition. *Palaeogeography, Palaeoclimatology, Palaeoecology* **204**, 353–72. doi: 10.1016/S0031-0182(03)00736-3.

Chen X, Zhang YD and Fan JX (2012) Onset of the Kwangsian Orogeny as evidenced by biofacies and lithofacies. *Science China: Earth Sciences* **55**, 1592–600. doi: 10.1007/s11430-012-4490-4.

Cooper RA, Rigby S and Loydell DK (2012) Palaeoecology of the Graptoloidea. *Earth Science Reviews* **112**, 23–41.

Craig H (1957) Isotopic standards for carbon and oxygen and correction factors for mass-spectrometric analysis of carbon dioxide. *Geochimica et Cosmochimica Acta* **12**, 133–49.

Cullers RL and Podkovyrov VN (2000) The geochemistry of shales, siltstones and sandstones of Pennsylvanian-Permian age, Colorado, USA: implications for provenance and metamorphic studies. *Lithos* **51**, 181–203.

De Baar HJW (1991) On cerium anomalies in the Sargasso Sea. *Geochimica et Cosmochimica Acta* **55**, 2981–3. doi: 10.1016/0016-7037(91)90463-F.

De Baar HJW, Bacon MP and Brewer PG (1985) Rare earth elements in the Pacific and Atlantic Oceans. *Geochimica et Cosmochimica Acta* **49**, 1943–59. doi: 10.1016/0016-7037(85)90089-4.

De Baar HJW, German CR and Elderfield H (1988) Rare earth element distributions in anoxic waters of the Cariaco Trench. *Geochimica et Cosmochimica Acta* **52**, 1203–19.

De Carlo EH and Green WJ (2002) Rare earth elements in the water column of Lake Vanda, McMurdo Dry Valleys, Antarctica. *Geochimica et Cosmochimica Acta* **66**, 1323–33. doi: 10.1016/S0016-7037(01)00861-4.

DePaolo DJ and Wasserburg GJ (1976) Nd isotopic variations and petrogenetic models. *Geophysical Research Letters* **3**, 249–52.

Dubois-Dauphin Q, Colin C, Bonneau L, Montagna P, Wu Q, Van Rooij D, Reverdin G, Douville E and Frank N (2017) Fingerprinting Northeast Atlantic water masses using neodymium isotopes. *Geochimica et Cosmochimica Acta*, **210**, 267–88.

Elderfield H (1988) The oceanic chemistry of the rare-earth elements. *Philosophical Transactions of the Royal Society of London* **325**, 105–26.

Elderfield H and Greaves MJ (1982) The rare earth elements in seawater. *Nature* **296**, 214–19. doi: 10.1038/296214a0.

Elias RJ and Young GA (1998) Coral diversity, ecology, and provincial structure during a time of crisis: the latest Ordovician to earliest Silurian Edgewood Province in Laurentia. *Palaios* **13**, 98–112.

Fan JX, Peng PA and Melchin MJ (2009) Carbon isotopes and event stratigraphy near the Ordovician–Silurian boundary, Yichang, South China. *Palaeogeography, Palaeoclimatology, Palaeoecology* **276**, 160–9.

Filippelli GM (2002) The global phosphorus cycle. In *Phosphates: Geochemical, Geobiological, and Materials Importance.* (eds MJ Kohn, J Rakovan, JM Hughes), pp. 391–425. Washington, DC: Mineralogical Society of America. Reviews in Mineralogy and Geochemistry 48.

Filippova A, Frank M and Kienast M (2017) Water mass circulation and weathering inputs in the Labrador Sea based on coupled Hf–Nd isotope compositions and rare earth element distributions. *Geochimica et Cosmochimica Acta* **199**, 164–84.

Finlay AJ, Selby D and Gröcke DR (2010) Tracking the Hirnantian glaciation using Os isotopes. *Earth and Planetary Science Letters* **293**, 339–48.

Finnegan S, Bergmann K and Eiler JM (2011) Magnitude and duration of Late Ordovician–Early Silurian glaciation. *Science* **331**, 903–6.

Föllmi KB (2016) Sedimentary condensation. *Earth-Science Reviews* **152**, 143–80.

Froelich PN, Klinkhammer GP and Bender ML (1979) Early oxidation of organic matter in pelagic sediments of the eastern equatorial Atlantic: suboxic diagenesis. *Geochimica et Cosmochimica Acta* **43**, 1075–90.

German CR and Elderfield H (1990) Application of the Ce anomaly as a paleoredox indicator: the ground rules. *Paleoceanography* **5**, 823–33

German CR, Holliday BP and Elderfield H (1991) Redox cycling of rare earth elements in the suboxic zone of the Black Sea. *Geochimica et Cosmochimica Acta* **55**, 3533–58

Ghienne JF (2003) Late Ordovician sedimentary environments, glacial cycles, and postglacial transgression in the Taoudeni Basin, West Africa. *Palaeogeography, Palaeoclimatology, Palaeoecology* **189**, 117–45.

Gorjan P, Kaiho K and David A (2012) Carbon- and sulfur-isotope geochemistry of the Hirnantian (Late Ordovician) Wangjiawan (Riverside) section, South China: global correlation and environmental event interpretation. *Palaeogeography, Palaeoclimatology, Palaeoecology* **337–338**, 14–22.

Gradstein FM, Ogg JG and Schmitz M (2012) *The Geologic Time Scale 2012.* Amsterdam: Elsevier, 1176 pp.

Hammarlund EU, Dahl TW and Harper DAT (2012) A sulfidic driver for the end-Ordovician mass extinction. *Earth and Planetary Science Letters* **331**, 128–39.

Hayashi K, Fujisawa H and Holland HD (1997) Geochemistry of ~1.9 Ga sedimentary rocks from northeastern Labrador, Canada. *Geochimica et Cosmochimica Acta* **61**, 4115–37.

Holmden C, Mitchell CE and LaPorte DF (2013) Nd isotope records of late Ordovician sea-level change: implications for glaciation frequency and global stratigraphic correlation. *Palaeogeography, Palaeoclimatology, Palaeoecology* **386**, 131–44.

Hu D, Zhang X, Zhou L Finney SC, Liu Y, Shen D, Shen M, Huang W and Shen Y (2017) $^{87}Sr/^{86}Sr$ evidence from the epeiric Martin Ridge Basin for enhanced carbonate weathering during the Hirnantian. *Scientific Reports* **7**, 11348. doi: 10.1038/s41598-017-11619-w.

Jones D, Martini A and Fike D (2017) A volcanic trigger for the Late Ordovician mass extinction? Mercury data from south China and Laurentia. *Geology* **45**, 631–4.

Kenneth G, Mac L and Ellen E (2008) Nd isotopic excursion across Cretaceous ocean anoxic event 2 (Cenomanian-Turonian) in the tropical North Atlantic. *Geology* **36**, 811–14. doi: 10.1130/G24999A.1.

Keto LS and Jacobsen SB (1987) Nd and Sr isotopic variations of Early Paleozoic oceans. *Earth and Planetary Science Letters* **84**, 27–41.

Keto LS and Jacobsen SB (1988) Nd isotopic variations of Phanerozoic paleooceans. *Earth and Planetary Science Letters* **90**, 395–410.

Kump LR and Arthur MA (1999) Interpreting carbon-isotope excursions: carbonates and organic matter. *Chemical Geology* **161**, 181–98.

LaPorte DF, Holmden C and Patterson WP (2009) Local and global perspectives on carbon and nitrogen cycling during the Hirnantian glaciation. *Palaeogeography, Palaeoclimatology, Palaeoecology* **276**, 182–95.

Laukert G, Frank M and Bauch D (2017) Transport and transformation of riverine neodymium isotope and rare earth element signatures in high latitude estuaries: a case study from the Laptev Sea. *Earth and Planetary Science Letters* **477**, 205–17.

Le Heron DP, Ghienne JF and Elhouicha M (2007) Maximum extent of ice sheets in Morocco during the Late Ordovician glaciation. *Palaeogeography, Palaeoclimatology, Palaeoecology* **245**, 200–26.

Li Y, Zhang T and Geoffrey S (2017) Depositional environment and organic matter accumulation of Upper Ordovician – Lower Silurian marine shale in the Upper Yangtze Platform, South China. *Palaeogeography, Palaeoclimatology, Palaeoecology* **466**, 252–64.

Liang D, Guo T and Chen J (2009) Some progresses on studies of hydrocarbon generation and accumulation in marine sedimentary region, southern China (part 2): geochemical characteristics of four suits of regional marine source rocks, South China. *Marine Origin Petroleum Geology* **14**, 1–15.

Lin J, Liu YS, Yang YH and Hu ZC (2016) Calibration and correction of LA-ICP-MS and LA-MC-ICP-MS analyses for element contents and isotopic ratios. *Solid Earth Sciences*, **1**, 5–27.

Ling H, Chen X and Li D (2013) Cerium anomaly variations in Ediacaran–earliest Cambrian carbonates from the Yangtze Gorges area, South China: implications for oxygenation of coeval shallow seawater. *Precambrian Research* **225**, 110–27.

Liu Y, Li C and Algeo TJ (2016) Global and regional controls on marine redox changes across the Ordovician-Silurian boundary in South China. *Palaeogeography, Palaeoclimatology, Palaeoecology* **463**, 180–91.

Luo G, Algeo TJ and Zhan R (2016) Perturbation of the marine nitrogen cycle during the Late Ordovician glaciation and mass extinction. *Palaeogeography, Palaeoclimatology, Palaeoecology* **448**, 339–48.

Ma YS, Chen HH and Wang GQ (2009) *Sequence Stratigraphy and Paleography in South China.* Beijing: Science Press, 591 pp.

McLennan SM, Fryer BJ and Young GM (1979) The geochemistry of the carbonate-rich Espanola Formation (Huronian) with emphasis on the rare earth elements. *Canadian Journal of Earth Sciences* **16**, 230–9.

McManus JM, Berelson WM and Coale KH (1997) Phosphorus regeneration in continental margin sediments. *Geochimica et Cosmochimica Acta* **61**, 2891–907.

Melchin MJ and Holmden C (2006) Carbon isotope chemostratigraphy in Arctic Canada: sea-level forcing of carbonate platform weathering and implications for Hirnantian global correlation. *Palaeogeography, Palaeoclimatology, Palaeoecology* **234**, 186–200.

Melchin MJ, Mitchell CE and Holmden C (2013) Environmental changes in the Late Ordovician–early Silurian: review and new insights from black shales and nitrogen isotopes. *Geological Society of America Bulletin* **125**, 1635–70.

Murry RW, Buchholtz BMR and Gerlach DC (1992) Interoceanic variation in the rare earth, major, and trace element depositional chemistry of chert: perspectives gained from the DSDP and ODP record. *Geochimica et Cosmochimica Acta* **56**, 1897–913.

Owen AW and Robertson DBR (1995) Ecological changes during the end-Ordovician extinction. *Modern Geology* **20**, 21–40.

Paikaray S, Banerjee S and Mukherji S (2008) Geochemistry of shales from the Paleoproterozoic to Neoproterozoic Vindhyan Supergroup: implications on provenance, tectonics and paleoweathering. *Journal of Asian Earth Sciences* **32**, 34–48.

Russell WA, Papanastassiou DA and Tombrello TA (1978) Ca isotope fractionation on the earth and other solar system materials. *Geochimica et Cosmochimica Acta* **42**, 1075–90.

Sageman BB, Murphy AE and Werne JP (2003) A tale of shales: the relative roles of production, decomposition, and dilution in the accumulation of organic-rich strata, Middle-Upper Devonian, Appalachian Basin. *Chemical Geology* **195**, 229–73.

Sandrine LeH, Laure M and Claude JA (2012) Nd isotope systematics on ODP Sites 756 and 762 sediments reveal major volcanic, oceanic and climatic changes in South Indian Ocean over the last 35 Ma. *Earth and Planetary Science Letters* **327–328**, 29–38.

Schachtman NS, Roering JJ, Marshall JA, Gavin DG and Granger DE (2019) The interplay between physical and chemical erosion over glacial-interglacial cycles. *Geology*, **47**, 613–16.

Schieber J (1992) A combined petrographical-geochemical provenance study of the Newland formation, Mid-Proterozoic of Montana. *Geological Magazine* **129**, 223–37.

Shields G and Stille P (2001) Diagenetic constraints on the use of cerium anomalies as palaeoseawater redox proxies: an isotopic and REE study of Cambrian phosphorites. *Chemical Geology* **175**, 29–48.

Sullivan N, Loydell D and Montgomery P (2018) A record of Late Ordovician to Silurian oceanographic events on the margin of Baltica based on new carbon isotope data, elemental geochemistry, and biostratigraphy from two boreholes in central Poland. *Palaeogeography, Palaeoclimatology, Palaeoecology* **490**, 95–106.

Tachikawa K, Jeandel C and Roy BM (1999) A new approach to the Nd residence time in the ocean: the role of atmospheric inputs. *Earth and Planetary Science Letters* **170**, 433–46.

Taylor SR and McLennan SM (1985) *The Continental Crust: Its Composition and Evolution*. Oxford: Blackwell, 312 pp.

Trotter JA, Williams IA and Barnes CR (2008) Did cooling oceans trigger Ordovician biodiversification? Evidence from conodont thermometry. *Science* **321**, 550–4.

Underwood CJ, Crowley SF, Marshall JD and Brenchley PJ (1997) High-resolution carbon isotope stratigraphy of the basal Silurian stratotype (Dob's Linn, Scotland) and its global correlation. *Journal of the Geological Society [London]* **154**, 709–18.

Wang X and Chai ZF (1989) Terminal Ordovician mass extinction and its relationship to iridium and carbon isotopes anomalies. *Acta Geologica Sinica* **3**, 255–64. (in Chinese)

Wei R, Abouchami W and Zahn R (2016) Deep circulation changes in the South Atlantic since the Last Glacial Maximum from Nd isotope and multi-proxy records. *Earth and Planetary Science Letters* **434**, 18–29.

Wilde P and Berry WBN (1984) Destabilization of the oceanic density structure and its significance to marine "extinction" events. *Palaeogeography, Palaeoclimatology, Palaeoecology* **48**, 143–62.

Wright J, Schrader H and Holser WT (1987) Paleoredox variations in ancient oceans recorded by rare-earth elements in fossil apatite. *Geochimica et Cosmochimica Acta* **51**, 631–44.

Yan C, Jin Z and Zhao J (2018) Influence of sedimentary environment on organic matter enrichment in shale: a case study of the Wufeng and Lungmachi Formations of the Sichuan Basin, China. *Marine and Petroleum Geology* **92**, 880–94.

Yan D, Chen D and Wang Q (2010) Large-scale climatic fluctuations in the latest Ordovician on the Yangtze block, south China. *Geology* **38**, 599–602.

Yan D, Chen D and Wang Q (2012) Predominance of stratified anoxic Yangtze Sea interrupted by short-term oxygenation during the Ordo-Silurian transition. *Chemical Geology* **291**, 69–78.

Yan D, Wang H and Fu Q (2015) Organic matter accumulation of Late Ordovician sediments in North Guizhou Province, China: sulfur isotope and trace element evidences. *Marine and Petroleum Geology* **59**, 348–58.

Yan DT, Chen DZ and Wang QC (2009) Carbon and sulfur isotopic anomalies across the Ordovician–Silurian boundary on the Yangtze Platform, South China. *Palaeogeography Palaeoclimatology Palaeoecology* **274**, 32–9.

Yang X, Yan D and Wei X (2018) Different formation mechanism of quartz in siliceous and argillaceous shales: a case study of Lungmachi Formation in South China. *Marine and Petroleum Geology* **94**, 80–94.

Young SA, Saltzman MR, Ausich WI, Desrochers A and Kaljo D (2010) Did changes in atmospheric CO_2 coincide with latest Ordovician glacial interglacial cycles? *Palaeogeography, Palaeoclimatology, Palaeoecology* **296**, 376–88.

Zhang G, Guo A and Wang Y (2013) Tectonics of South China continent and its implications. *Science China Earth Sciences* **56**, 1804–28.

Zhou L, Algeo TJ and Shen J (2015) Changes in marine productivity and redox conditions during the Late Ordovician Hirnantian glaciation. *Palaeogeography, Palaeoclimatology, Palaeoecology* **420**, 223–34.

Zou C, Qiu Z, Poulton SW, Dong D, Wang H, Chen D, Lu B, Shi Z and Tao H (2018) Ocean euxinia and climate change "double whammy" drove the Late Ordovician mass extinction. *Geology* **46**, 535–8.